Monthly Notices
of the
ROYAL ASTRONOMICAL SOCIETY

MNRAS **496,** 550–563 (2020)
Advance Access publication 2020 May 28

doi:10.1093/mnras/staa1476

# Eclipsing binaries in the *OGLE* variable star catalogue: long-period evolved systems

Barış Hoyman ,★ Sara Bulut , Orkun Özdarcan and Ömür Çakırlı

*Ege University, Science Faculty, Astronomy and Space Science Dept, 35100 Bornova, İzmir, Turkey*

Accepted 2020 May 16. Received 2020 May 16; in original form 2020 January 10

## ABSTRACT

Red giant stars are proving to be an exceptional source of information for testing models of stellar evolution, as photometric and spectroscopic analysis has opened up a window into their interiors, providing an exciting chance to develop highly constrained stellar models. In this study, we present a determination of precise fundamental physical parameters belonging to five detached, double-lined, eclipsing binary stars in the Large and Small Magellanic Clouds containing G- or early K-type giant stars with extended envelopes. We also derived the distances to the systems by using a temperature–colour relation and compared these distances with the measurements provided in the literature. The measured stellar masses are in the range 1.8–3.0 $M_{\odot}$ and comparison with the PAdova and TRieste Stellar Evolution Code (PARSEC) isochrones gives ages between 0.4 and 1.1 Gyr. The derived uncertainties for individual masses and radii of components are better than 3 and 7 per cent, respectively, for these systems. Additionally, we performed atmospheric parameter determination and [*M*/H] analysis for each, where we disentangled the spectra.

**Key words:** binaries: eclipsing – binaries: spectroscopic – stars: evolution – stars: fundamental parameters – stars: late-type .

## 1 INTRODUCTION

Since 1996, the Optical Gravitational Lensing Experiment (*OGLE*) mission has observed the southern skies continuously and measured the flux for thousands of stars. It is observing the densest regions in the southern sky and collecting time-domain photometric data of a billion stars (Wyrzykowski et al. 2019). Among its main achievements are discoveries of a million variable stars, a few dozen extrasolar planets, supernovae, black hole candidates, thousands of quasars and thousands of microlensing events. It has made a remarkable contribution to the studies of red giants in eclipsing binaries (hereafter RG/EBs) with an extended envelope.

Up to now, a number of red giant stars that are members of binary systems have been detected in different space survey data (Hekker et al. 2010; Beck et al. 2014; Gaulme et al. 2014, 2013, 2016), with orbital periods varying from 19–1058 days. In these remarkable surveys, eclipse and radial velocity modelling was used to derive the orbital and dynamical stellar parameters. Additionally, masses and radii of the RG/EB components were calculated by utilizing the asteroseismic scaling relations. In a deep comparison between the outcomes from exhaustive binary modelling and asteroseismology, Gaulme et al. (2016) demonstrated that the stellar masses and radii calculated using asteroseismic scaling correlations are systematically overestimated.

To explore further, it is essential to study some RG/EBs in greater detail. By using high-resolution spectra with light curves, we can characterize RG/EBs orbital dynamics properly, measure component masses and radii, reveal their atmospheric parameters and investigate their evolutionary backgrounds. In Table 1, we summarize some basic parameters for five RG/EBs that are the subject of this study. We have the best study samples of stars, which can begin to address the connections between orbital parameters and tidal synchronization time-scales and are of prime importance to test stellar evolution histories in the context of binarity. Consequently, we decided to investigate systems with high-resolution spectroscopy and light-curve data. In this article, we present physical parameters for the unique RG/EBs with a combination of dynamical and stellar atmosphere modelling. In Section 2, we briefly discuss literature information about the targets and in Section 3 we describe how we acquired and processed photometric and spectroscopic data. Section 4 explains our radial velocity extraction process, light-curve analysis and how we obtained atmospheric parameters from disentangled spectra, where we calculated each star's contribution to the spectra to perform stellar atmosphere modelling. We then present the evolutionary status of the RG/EBs in Section 5. Finally, detailed conclusions are presented in Section 6.

★ E-mail: barishoyman@gmail.com

**Table 1.** Literature information about the targets from this work.

| *OGLE* name | $\alpha_{2000}$ | $\delta_{2000}$ | $P$ (d)[a] | $T_0$ (BJD −245 0000)[a] | $V$(mag)[b] |
|---|---|---|---|---|---|
| OGLE LMC-ECL-02197 | 04:53:14.68 | −67:33:59.04 | 199.7569602 | 7102.02720 | 17.409 |
| OGLE LMC-ECL-33491 | 05:27:00.64 | −67:29:09.91 | 737.9910007 | 7462.34220 | 18.533 |
| OGLE SMC-ECL-03529 | 00:57:05.35 | −73:15:10.81 | 234.4566935 | 7149.41460 | 17.742 |
| OGLE SMC-ECL-00439 | 00:40:21.45 | −73:27:19.49 | 279.4045331 | 7126.36310 | 18.066 |
| OGLE SMC-ECL-00727 | 00:44:12.10 | −73:17:42.00 | 316.6270355 | 7033.80350 | 18.116 |

[a]For the eclipsing binary, where $T_0$ is the primary eclipse mid-time (http://ogledb.astrouw.edu.pl/).
[b]*OGLE*-IV Johnson–Cousins filters.

## 2 TARGETS

The eclipsing nature of all targets in the Large Magellanic Cloud (LMC) and Small Magellanic Cloud (SMC) was discovered by the *OGLE* mission (Pawlak et al. 2016). The *OGLE* database includes over 40 million stars, with photometric data accessible to the public. It contains 48 605 eclipsing binary systems, 40 204 belonging to the LMC and 8401 to the SMC. Pawlak et al. (2016) presented the time-series photometry obtained for selected objects during the fourth phase of the *OGLE* project. By selecting the number of existing data points for a particular star, the quality of the statistics and the differences between average and median intensity, it is possible to extract candidate stars that could be eclipsing binaries. The candidates were first scrutinized by searching the Simbad Database (Wenger et al. 2000) to see if these stars have already been determined to be eclipsing variables or variables in general. All of them have been exposed as eclipsing binaries by the *OGLE* Eclipsing Stars Database,[1] but none of them has been studied spectroscopically until now. This is the first study of these systems. The targets offered in this study are summarized in Table 1. For each of them, no literature data, except for brightness and position measurements, are available and neither light-curve solutions nor radial velocity studies have been attempted so far.

## 3 OBSERVATIONS

*OGLE* is in the category of extended-running large-scale photometric sky surveys focused on variability. This survey uses a dedicated 1.3-m telescope built in 1996, placed at Chile's Las Campanas Observatory (run by the Carnegie Institution for Science). Its original goal was detecting microlensing events and thus it observes high-density stellar fields. Now in *OGLE*–IV phase, the telescope used for *OGLE* has been equipped with a mosaic camera with a 1.4 deg$^2$ field of view since 2010. A detailed description of *OGLE*–IV can be found in Udalski, Szymański & Szymański (2015). The whole sky field covered is about 3500 deg$^2$ and this contains about 1.3 billion sources located in the Galactic bulge, Galactic disc and Magellanic Clouds, the densest stellar regions of the southern sky.

### 3.1 *OGLE* photometry

*V*- and *I*-band interference filter sets are used on the *OGLE*-IV camera. The *OGLE I*-band filter is very similar to the standard *I*-band filter; the *OGLE*-IV *V*-band filter is similar to the standard Johnson filter but does not extend as much into the red (Udalski et al. 2015). The *I* filter was used to perform most observations and the light curves thus obtained contain from hundreds to more than a thousand data points and an integration time of 100 s. The *OGLE*-IV photometry covers the range $12 < I < 20.5$ mag (Udalski et al. 2015). Light curves and the ephemeris for each star are published in different catalogues. Recently, the *OGLE* team updated the list of eclipsing binaries in the Magellanic Clouds with new results from the *OGLE*–IV project (40 204 sources in the LMC and 8401 sources in the SMC: Pawlak et al. 2016). In our study we used *V*- and *I*-band optical photometry for the systems obtained during the fourth phase of the *OGLE* project. The phase coverage for the light curves is complete in both filters.

### 3.2 Spectroscopic data

There have been spectroscopic observations of the target areas over a very long period of time, and there is a large database of these observations from different telescope/spectrograph combinations spanning almost five years. As in previous similar work (Hoyman et al. 2019), our high-resolution (processed) spectra at optical wavelengths were retrieved from the European Southern Observatory (ESO) Science Archive Facility[2] and from observations performed with the Ultraviolet and Visual Echelle Spectrograph (UVES) installed on the ESO Very Large Telescope Unit Telescope 2 (VLT/UT2; Kueyen) telescope ($R \simeq 50\,000$) through the Fibre Large Array Multi Element Spectrograph (FLAMES) system located at Paranal Observatory and the High Accuracy Radial velocity Planet Searcher (HARPS) spectrograph attached to the ESO 3.6-m telescope ($R \simeq 80\,000$, in Extra Good General Spectroscopy (EGGS) mode) located at La Silla observatory. While spectra belonging to four stars were taken from the archive of the UVES, one star's spectra were obtained from both HARPS and UVES (see Appendix, Table A1). We used the wavelength-calibrated 1D spectra product from a dedicated pipeline, as reduced by ESO personnel. The ESO spectra are described further in the ESO archive and the archive also provides details regarding the retrieval of spectra.

## 4 ANALYSIS

### 4.1 Radial velocity measurements and orbital solutions

To construct the orbital solutions of the systems, we first derived the radial velocities of both components for each system. For this purpose we used the cross-correlation technique (CCT: Simkin 1974; Tonry & Davis 1979), which is commonly used and implemented in the RAVESPAN application (Pilecki et al. 2013,

[1]http://ogledb.astrouw.edu.pl/~ogle/OCVS/

[2]Based on spectra from observations made with ESO telescopes at La Silla and Paranal Observatories under programs 094.D-0056(A), 095.D-0424(A), 097.D-0150(A), 0100.D-0273(A) by Gieren, W., 092.D-0363(A), 096.D-0425(A), 097.D-0400(A), 098.D-0263(A), 0100.D-0339(A), 0100.D-0339(B) by Pietrzynski, G.

2015). The spectra of the eclipsing binaries were cross-correlated against synthetic spectra (further information regarding generating synthetic spectra is given in Section 4.3). We provide the orbital solutions in Fig. 1. The bottom panel of each orbital solution shows the measured radial velocities for the primary and secondary (fitted orbital solutions in different colours). The best-fitting models are plotted with continuous lines for primary and secondary eclipses. The orbital elements are listed in Table 2, which contains the binary ID, date of periastron passage ($T_0$), orbital period ($P$), eccentricity ($e$), argument of periastron ($\omega$), centre-of-mass $RV$ ($\gamma$), orbital amplitude of the components ($K_{1,2}$), $M_{1,2} \sin^3 i$, projected semimajor axis ($a \sin i$), root-mean-square (rms) residual velocity for the primary and secondary from the orbital solution and number of radial velocity measurements ($N$) for radial velocity analysis. The resultant heliocentric radial velocities for the primary ($V_p$) and secondary ($V_s$) components are listed in Table A1, along with the dates of observations. The $\sigma_i$ values are computed according to the fitted peak height, as described by Tonry & Davis (1979). We note that the $\sigma_i$ values of HARPS spectra are larger than those of UVES spectra, due to the relatively low signal-to-noise ratio (S/N).

### 4.2 Light-curve modelling

With the radial velocity measurements of the systems at hand, we proceeded to fit the *OGLE* light curves. Modelling of the eclipsing binaries' light curves was performed with the publicly available code JKTEBOP (v34:[3] Southworth, Maxted & Smalley 2004; Southworth et al. 2004), which relies on the Nelson–Davis–Etzel biaxial ellipsoidal model. We note that this software is appropriate for detached EBs where tidal distortion is negligible. It is based on the EBOP code (Popper & Etzel 1981), originally written by Paul Etzel and based on the model of Nelson & Davis (1972). It is a quick procedure that analyses photometric data one set at a time and, in the version used for this article, did not allow for spots or pulsations.

The initial values of eccentricity $e$ and periastron longitude $\omega$, as well as mass ratio $q$ (here kept fixed), were taken from RAVESPAN runs (see previous section). We fitted for the orbital period $P$, mid-time of the primary (deeper) minimum $T_0$, sum of the fractional radii $r_1 + r_2$ (where $r = R/a$), their ratio $k = r_2/r_1$, orbital inclination $i$, surface brightness ratio $J$ and light scalefactor $S$, as well as for $e$ and $\omega$. The gravity-darkening coefficients and bolometric albedos were always kept fixed at the values appropriate for stars with convective envelopes ($g = 0.32$, $A = 0.5$; Ruciński 1969). The quadratic limb-darkening (LD) law (Kopal 1950) with approximate coefficients was taken from the tables of Claret (2000). After more iteration, we determined that using slightly inaccurate limb-darkening coefficients does not have a significant effect on the errors of the final solution-based parameters for the *OGLE* data. The solutions obtained for the photometric measurements are presented in Fig. 1, upper panel. Table 2 shows the mean formal errors in photometric measurements, orbital fitting RMS and multiplicative factors for the systems analysed.

JKTEBOP uses the Levenberg–Marquardt (LM) optimization method to find the best-fitting model for a light curve. The general approach to finding the formal uncertainties in parameters returned by the LM minimization algorithm in light-curve modelling involves calculating from the solution covariance matrix and is an inadequate representation of the overall parameter uncertainties, particularly while some parameters are strongly correlated (Popper 1984; Southworth & Clausen 2007). For that reason, LM minimization has been ignored in this work. In order to calculate the random errors in the initial values of parameters, we used the Monte Carlo simulation algorithm implemented in JKTEBOP, which was found to quantify the correlations between parameters. For each $I$-band observed light curve, a 'synthetic' light curve was constructed by evaluating the best-fitting model at the phases of observation. This process was undertaken 10 000 times for each observed light curve of the system. The standard deviation of the distribution of values for each parameter has been calculated. A sample plot of the distributions of different parameter values for OGLE LMC-ECL-2197 is shown in Fig. 2.

### 4.3 Atmospheric parameters from disentangled spectra

A detailed spectroscopic analysis of the evolved eclipsing binary systems was planned to figure out the fundamental atmospheric parameters, abundances and projected rotational velocity ($v \sin i$) values of the components of the systems. Therefore, after analysis of the radial velocity and light curves, the atmospheric parameters were obtained from the disentangled spectra.

Because the observed spectra of double-lined binaries show a composite spectrum of two component's signals, an important complexity arises when trying to fit synthetic spectra to those observed spectra. It is possible to acquire separate spectra for each component by disentangling the signals using well phase-covered observational epochs. The disentangled spectra are equal to the intrinsic component spectra multiplied by the respective light factors, i.e. the fractional light contribution of the components to the total light of a binary system. This can be achieved with a type of spectral disentangling technique. Although there are several different codes appropriate for this problem, we prefer the FDBINARY[4] code, since it is user-friendly and open source. The code combines Fourier techniques with the orbital parameters and radial velocities of the components in order to disentangle the spectra (Ilijic et al. 2004). Although the FDBINARY code allows for three-component disentangling and light-ratio variations by phase, as we have explained below, the only basis in this study is the calculation of light-ratio changes of the two components with respect to the orbital phase. In application of the spectral disentangling method, we used the spectral interval 5100–5200 Å. It has been well known for a long time that strong lines with marked wings can be useful tracers of the $\log(g)$ parameter, since stars with extended atmospheres provide much less support for collisional broadening (Gray 1992). Cayrel de Strobel (1969) introduced the Mg Ib triplet lines as one of the best gravity criteria for stars and Fuhrmann et al. (1997) utilized the pressure-dependent Mg Ib lines λ5172 and λ5183 in $\epsilon$ Virginis (G8III) as gravity indicators.

In the analysis, the spectra with the lowest S/N ratios were not used. The derived orbital parameters were used as inputs. The values of orbital period $P$, time of minimum light $T_0$, orbital eccentricity $e$ and argument of periastron $\omega$ were fixed parameters in the analysis. After the disentangled spectra of each spectral part were obtained, they were renormalized considering the light ratio of components obtained from the initial light-curve analysis. In this process, the procedure given by Ilijic (2004) was used.

For this step of our work, the main motivation was to calculate the atmospheric parameters, which are the key parameters to determine

[3] https://www.astro.keele.ac.uk/jkt/codes/jktebop.html

[4] http://sail.zpf.fer.hr/fdbinary/

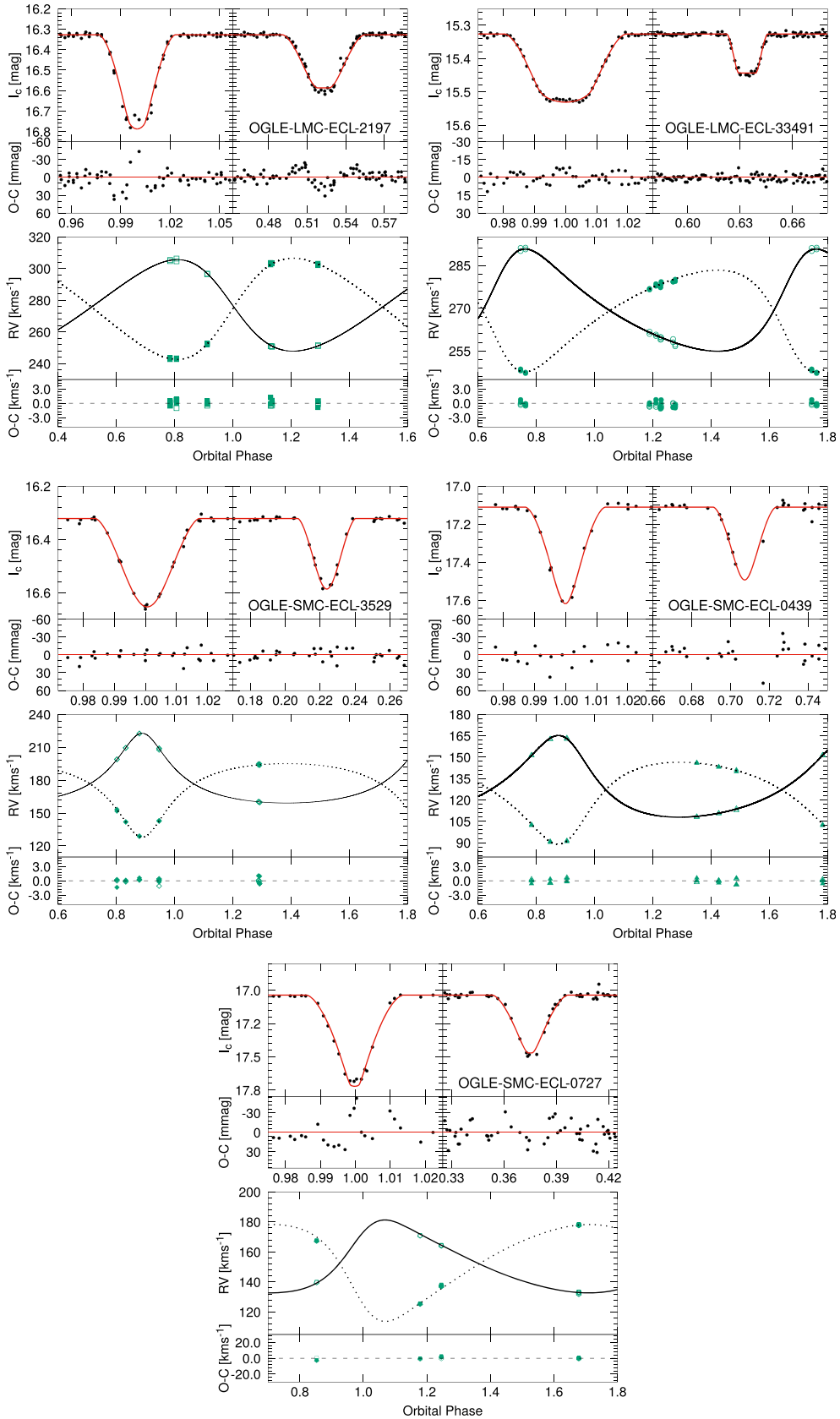


**Figure 1.** Joint fits to the *OGLE* photometry and radial velocity time series of target stars. The upper left and right panels show the primary and secondary eclipses, respectively. The best-fitting models are plotted with continuous lines. Filled symbols on the RV plot refer to the primary and open symbols to the secondary. The LC model is fitted to the complete *I*-band *OGLE* photometry light curves. Phase '1.0' is for the deeper eclipse mid-time.

**Table 2.** Binary parameters of systems. Errors in units of the last digits are given in parentheses. $l_2/l_1$, $M_{bol}$, $(m–M)_V$ and $d$ denote the luminosity ratio, absolute bolometric magnitude, distance modulus and distance, respectively.

| Parameter | OGLE LMC-ECL-02197 | | OGLE LMC-ECL-33491 | | OGLE SMC-ECL-03529 | | OGLE SMC-ECL-00439 | | OGLE SMC-ECL-00727 | |
|---|---|---|---|---|---|---|---|---|---|---|
| | Primary | Secondary | Primary | Secondary | Primary | Secondary | Primary | Secondary | Primary | Secondary |
| $T_0$ (HJD−2, 400 000)[a] | 57102.0267(5) | | 57883.4089(5) | | 57202.0945(7) | | 57126.0021(3) | | 57152.8494(1) | |
| $P$ (day) | 199.749116(14) | | 948.504312(59) | | 234.447821(31) | | 279.333357(49) | | 316.687975(37) | |
| RV analysis | | | | | | | | | | |
| $\gamma$ (km s$^{-1}$) | 275.7(7) | | 268.3(1.1) | | 176.7(5) | | 127.1(1.2) | | 152.2(7) | |
| $e$ | 0.166(11) | | 0.325(17) | | 0.450(7) | | 0.353(11) | | 0.295(11) | |
| $\omega$ (°) | 78(1) | | 309(3) | | 359(4) | | 21(2) | | 311(5) | |
| $q$ | 0.906(23) | | 1.004(35) | | 0.947(13) | | 0.996(18) | | 0.752(14) | |
| $a \sin i$ (R$_\odot$) | 236.1(1.3) | | 633.9(3.9) | | 270.3(2.1) | | 296.4(1.9) | | 338.9(1.6) | |
| $M_{1,2} \sin^3 i$ (M$_\odot$) | 2.329(10) | 2.102(30) | 1.905(56) | 1.899(64) | 2.479(11) | 2.349(21) | 2.245(26) | 2.236(28) | 2.974(29) | 2.238(21) |
| $K_{1,2}$ (km s$^{-1}$) | 28.9(9) | 31.9(8) | 17.9(8) | 17.9(9) | 31.8(1) | 33.6(1) | 28.6(3) | 28.8(7) | 24.3(5) | 32.3(6) |
| $rms_{RV_{1,2}}$ (km s$^{-1}$) | 0.41 | 0.44 | 0.44 | 0.43 | 0.44 | 0.45 | 0.41 | 0.52 | 0.51 | 0.51 |
| $N_{RV}$ | 12 | | 16 | | 13 | | 12 | | 8 | |
| JKTEBOP analysis | | | | | | | | | | |
| $i$(°) | 88.4(7) | | 89.2(6) | | 86.6(4) | | 88.3(7) | | 89.5(9) | |
| $r_{1,2}$ | 0.1069(14) | 0.0662(21) | 0.0101(7) | 0.0097(9) | 0.0486(5) | 0.0365(8) | 0.0345(7) | 0.0350(8) | 0.0496(5) | 0.0607(6) |
| $J$ | 0.698(6) | | 0.700(9) | | 0.639(12) | | 0.909(9) | | 0.675(11) | |
| $l_2/l_1$ | 0.787 | | 0.881 | | 0.698 | | 0.597 | | 0.670 | |
| $X^b_{1,2}$ | 0.3587 | 0.3612 | 0.1983 | 0.2107 | 0.2271 | 0.2647 | 0.2814 | 0.3005 | 0.2516 | 0.2839 |
| $Y^b_{1,2}$ | 0.2739 | 0.2659 | 0.3479 | 0.3427 | 0.3386 | 0.3193 | 0.3111 | 0.3008 | 0.3249 | 0.3121 |
| Atmospheric analysis | | | | | | | | | | |
| $T_{eff\,1,2}$ (K) | 4 750(120) | 4 800(220) | 5 800(180) | 5 700(170) | 5 500(180) | 5 300(250) | 5 200(220) | 5 100(220) | 5 400(150) | 5 200(150) |
| log ($g_{1,2}$) (cgs) | 2.20(21) | 2.80(32) | 3.25(46) | 3.40(14) | 2.95(51) | 3.00(53) | 2.95(47) | 3.00(51) | 2.6(2) | 2.4(2) |
| ($v_{mic.}$) (km s$^{-1}$) | 1.19 | 1.86 | 1.43 | 1.31 | 1.57 | 1.64 | 1.43 | 1.44 | 2.13 | 2.99 |
| ($v_{mac.}$) (km s$^{-1}$) | 4.0 | 4.91 | 5.55 | 4.16 | 5.42 | 4.27 | 5.45 | 5.55 | 5.95 | 6.31 |
| $(v_{1,2} \sin i)_{obs}$ (km s$^{-1}$)[d] | 6.5(1) | 11.9(5) | 7.7(5) | 10.8(7) | 6.8(8) | 11.9(8) | 4.5(9) | 5.4(1.1) | 7.2(4) | 7.9(7) |
| [$M$/H] | −0.44(4) | −0.48(9) | −0.35(5) | −0.31(8) | −0.51(12) | −0.27(33) | −0.55(7) | −0.61(9) | −0.50(25) | −0.50(25) |
| Reduced $\chi^2$ | 0.0167 | 0.0554 | 0.0278 | 0.0034 | 0.0164 | 0.0430 | 0.0019 | 0.0306 | 0.0081 | |
| Absolute parameters | | | | | | | | | | |
| $M_{1,2}$ (M$_\odot$) | 2.33(9) | 2.10(10) | 1.90(13) | 1.89(14) | 2.49(9) | 2.36(10) | 2.25(9) | 2.24(10) | 2.97(11) | 2.24(13) |
| $R_{1,2}$ (R$_\odot$) | 25.25(16) | 15.64(19) | 6.40(52) | 6.15(55) | 13.16(67) | 9.88(88) | 10.23(38) | 10.38(88) | 16.81(54) | 20.57(89) |
| log ($g_{1,2}$) (cgs) | 2.00(11) | 2.37(17) | 3.10(21) | 3.14(35) | 2.60(21) | 2.82(33) | 2.77(7) | 2.76(9) | 2.46(4) | 2.16(6) |
| log ($L_{1,2}$/L$_\odot$) | 2.46(9) | 2.08(11) | 1.621(224) | 1.557(357) | 2.155(64) | 1.842(101) | 1.839(104) | 1.818(126) | 2.236(67) | 2.307(77) |
| $(v_{1,2} \sin i)_{calc}$ (km s$^{-1}$)[c] | 6.4(6) | 4.0(5) | 1.0(3) | 1.0(5) | 2.8(2) | 2.1(3) | 2.8(2) | 2.9(2) | 2.7(1) | 3.3(2) |
| log $\tau_{circ}$ (yr) | 17.74(1) | | 21.38(1) | | 18.12(1) | | 18.54(1) | | 18.75(1) | |
| $r_{peri}$ (R$_\odot$) | 196.99(13) | | 427.96(11) | | 148.94(10) | | 191.83(17) | | 238.91(15) | |
| $E(V–I)$ (mag)[e] | 0.05(7) | | 0.08(6) | | 0.03(4) | | 0.01(3) | | 0.02(4) | |
| $E(B–V)$ (mag)[e] | 0.078(7) | | 0.099(5) | | 0.063(6) | | 0.048(3) | | 0.049(4) | |
| $d$ (kpc)[e] | 43.4(1.2) | | 42.7(0.9) | | 44.4(2.3) | | 45.3(2.2) | | 45.5(1.4) | |
| $M_{bol}$ (mag) | −1.42(24) | −0.47(25) | 0.70(14) | 0.86(23) | −0.63(24) | 0.14(27) | 0.15(20) | 0.21(21) | −0.84(15) | −1.02(19) |
| $(m–M)_V$ (mag) | 18.43(21) | 18.31(25) | 18.38(14) | 18.12(23) | 18.56(24) | 18.47(27) | 18.44(20) | 18.32(21) | 18.74(15) | 18.70(19) |
| $E(B–V)$[f] (mag) | 0.095(11) | | 0.119(15) | | 0.088(17) | | 0.101(23) | | 0.123(44) | |
| $d$ (kpc)[f] | 53.5(2.1) | | 45.9(1.9) | | 48.2(2.4) | | 44.9(2.8) | | 56.7(3.4) | |

[a]Mid-time of the primary (deeper) eclipse, calculated from the complete light curve.
[b]$X$ and $Y$, linear and non-linear coefficients of limb darkening, respectively.
[c]The velocity of (pseudo) synchronous components given by JKTABSDIM.
[d]$v_{1,2}$ calculated with ISPEC.
[e]Calculated from Haschke, Grebel & Duffau (2011).
[f]Calculated from Di Benedetto (2005).

the age and evolutionary status of the binary components, from the disentangled spectra. We used the freely distributed ISPEC code ($v$2019.03.02: Blanco-Cuaresma et al. 2014)[5] for this purpose. In order to provide the atmospheric parameters, we used the spectral synthesis approach, employing the code SPECTRUM (Gray & Corbally 1994), the Model Atmospheres in Radiative and Convective Scheme (MARCS) grid of model atmospheres (Gustafsson et al. 2008), solar abundances from Grevesse, Asplund & Sauval (2007) and the atomic line list provided by the third version of the Vienna atomic line database (VALD3: Ryabchikova et al. 2015). ISPEC uses 'segments', which are certain, user-defined ranges to synthesize spectra. We defined 100-Å segments around certain lines, which is the default approach. We run the fit with the following parameters set free: effective temperature $T_{eff}$, gravity log ($g$), metallicity [$M$/H] and rotational velocity $v \sin i$. The resolution $R$ was always fixed to 50 000. Lines of systems are quite narrow, so macro- and microturbulence velocities $v_{mic}$, $v_{mac}$ were calculated automatically by ISPEC from an empirical relation found by Sheminova (2019)

[5]https://www.blancocuaresma.com/s/iSpec

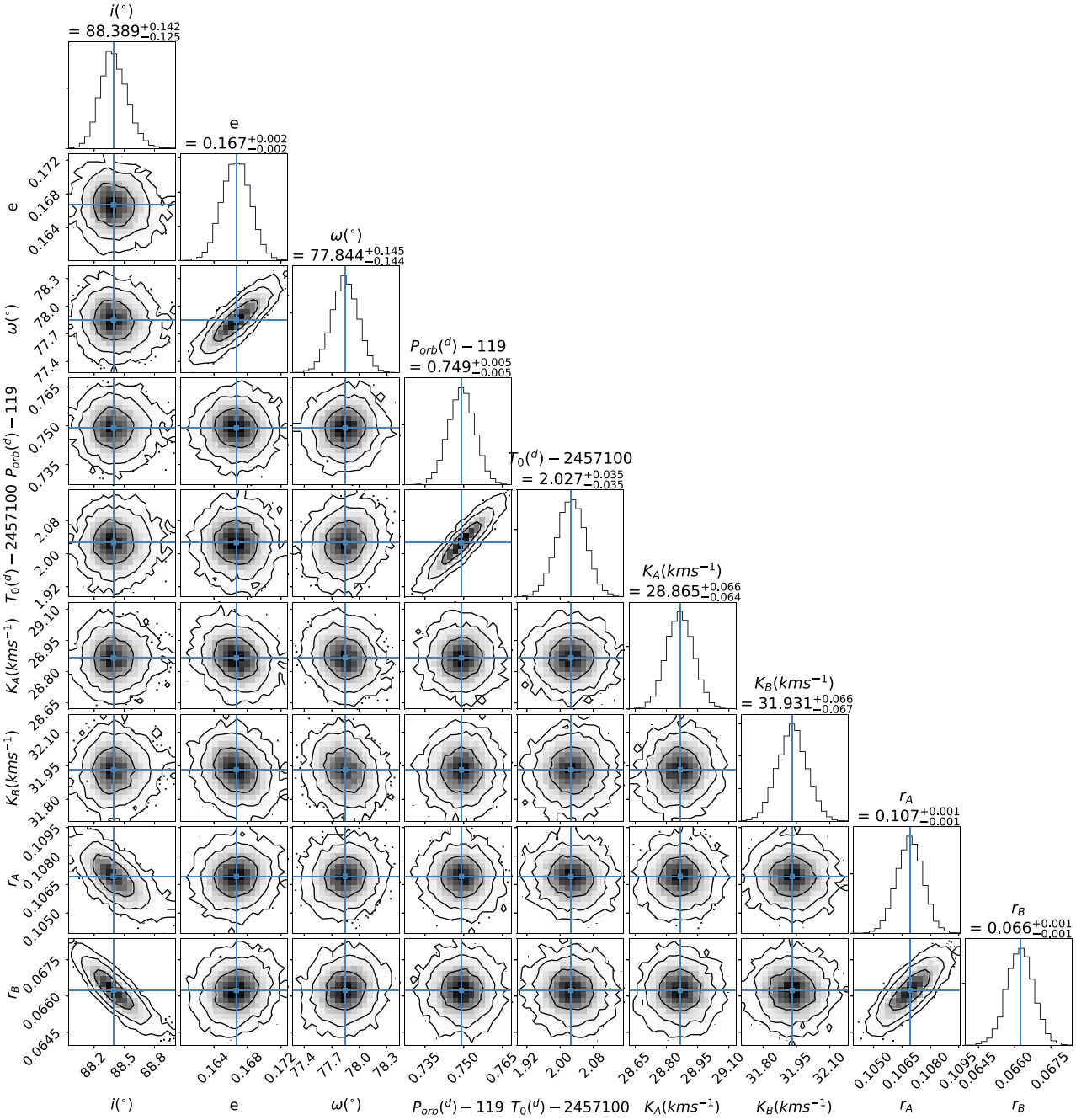


**Figure 2.** 'Corner plot' (Foreman-Mackey (2016); source code available at https://github.com/dfm/corner.py) for OGLE LMC-ECL-2197, illustrating the correlations among the main fit parameters of our solution. Contour levels correspond to 1, 2 and 3$\sigma$ and the histograms on the diagonal represent the posterior distribution for each parameter, with the mode and internal 68 per cent confidence levels indicated. More realistic errors are discussed in the text.

and incorporated into the ISPEC program. This method works without problem, except for OGLE SMC-ECL-00727, where we were not able to disentangle the composite spectra of the system due to an insufficient number of observed spectra. Thus, we computed a grid of stellar synthetic spectra and combined them by considering radial velocities and the radius ratio of the components for OGLE SMC-ECL-00727. In synthetic spectrum calculation, we adopted the same radiative transfer code, model atmosphere and line list as in ISPEC calculations on disentangled spectra. We computed grids for a temperature range between 5000 and 5500 K, $\log(g)$ range between 2.0 and 3.5 and metallicity range between 0 and −1.0. Grid steps of the synthetic spectra were 100 K in temperature, 0.1 in logarithm of the surface gravity and −0.25 in overall metallicity ([*M*/H]). We used the IDL code BINMAG,[6] written by Oleg Kochukhov, to apply this method. The method can be summarized as follows: considering preliminary light-curve modelling results, we adopted temperatures and $\log(g)$ values for each component and computed a synthetic spectrum for each one.

[6]https://www.astro.uu.se/~oleg/binmag.html

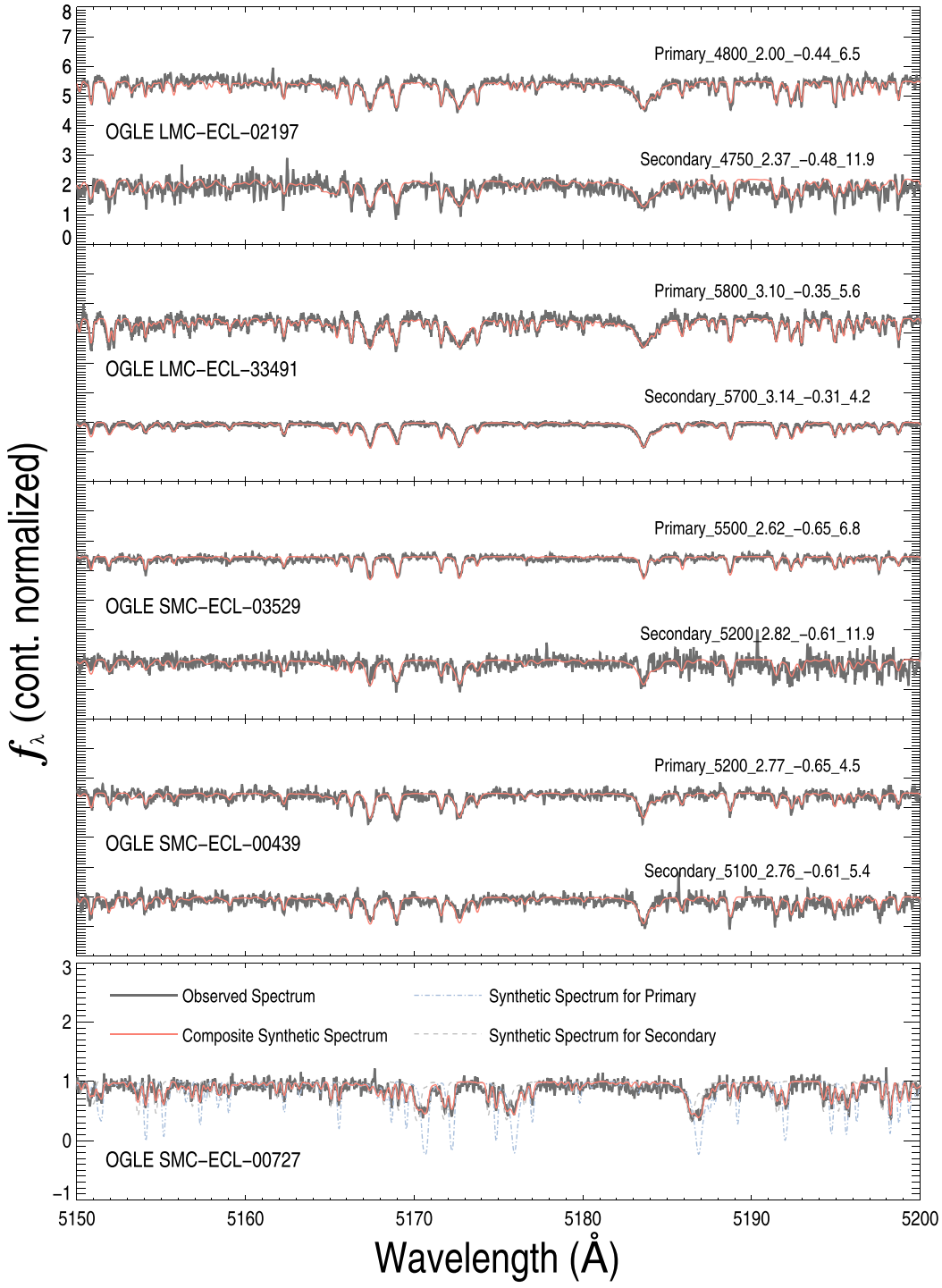


**Figure 3.** Illustration of the spectral disentangling procedure in the 5150–5200 Å wavelength region. The observed spectra are shown with the thick lines. The continuous lines over the observed spectra correspond to the model spectra with system name; Component_$T_{\rm eff}$ (K)_log($g$)(cgs)_[$M$/H] (dex)_$v \sin i$ (km s$^{-1}$).

Then we produced the composite spectrum of the target system by combining computed spectra with respect to the radial velocities and radius ratio of the components. Finally, we compared observed and computed composite spectra. Considering preliminary light-curve modelling results, we obtained synthetic composite spectra of the system for different atmospheric parameter combinations. Comparing synthetic composite spectra computed for different combinations with the observed composite spectrum, we found the synthetic spectrum with the smallest reduced $\chi^2$ value and listed final atmospheric parameters in Table 2. We estimated the uncertainty of temperature, log ($g$) and metallicity as 150 K, 0.2 and 0.25, respectively.

The full optimized parameters are listed in Table 2. An application of this disentangling procedure is illustrated in Fig. 3 for the 5100–

5200 Å region. This figure shows individual disentangled spectra and the final fit of the primary and secondary components. In the case of OGLE SMC-ECL-00727, the lowermost panel of the figure shows the observed composite spectrum and best-fitting synthetic composite spectrum.

### 4.4 Absolute dimensions

To compute the absolute values of stellar parameters, the partial outcomes of light curves and radial velocity solutions were combined using the JKTABSDIM[7] code (Southworth, Maxted & Smalley 2005), available together with JKTEBOP. As input parameters, this basic procedure takes orbital period ($P$), eccentricity ($e$), fractional radii ($r_{1,2}$), velocity semi-amplitudes ($K_{1,2}$) and inclination ($i$) (all with formal uncertainties) and returns absolute values of masses and radii (in solar units), log ($g$) and rotational velocities, assuming tidal locking and synchronization. The code can also calculate the distance to targets, using effective temperatures of two components, approximate metallicity, $E(B–V)$ and apparent magnitudes via various calibrations. We note that log ($g$) values found from atmospheric analysis differ from light and radial velocity modelling results by ∼0.25. This is not an unexpected difference, since atmosphere analysis based on synthetic spectrum calculation is not as robust as combined light-curve and radial velocity modelling against log ($g$) values.

#### 4.4.1 *Extinction*

Extinction determination methods for eclipsing binaries are very flexible and there are many different approaches. Of these methods, up to now, the most popular and extensively used source for dealing with extinction, used for determination of the distances to the Magellanic Clouds, was the reddening map for the Magellanic Clouds obtained from the analysis of red clump stars (Haschke et al. 2011) on the basis of *OGLE* data. We calculated the colour excess using the equation

$$E(B-V) = \frac{E(V-I)}{1.3} + 0.057,$$

where $E(V–I)$[8] is the colour excess from the reddening map, the denominator of 1.3 is adopted from Bessell, Castelli & Plez (1998), and $\Delta E(B–V) = 0.057$ mag is the foreground Galactic reddening in the direction of the systems as derived from the dust maps of Schlafly & Finkbeiner (2011). Using the method described above, we determined the reddening towards our targets ($E(B–V)$ values, see Table 2), which is approximately equal towards the direction of LMC and SMC stars (Pietrzyński et al. 2019; Zaritsky et al. 2002).

Besides the calibrations explained above, we also estimated the reddening from the recalibration of extinction maps from Schlafly & Finkbeiner (2011) and 3D Dust Mapping, which is based on Pan–STARRS 1 photometry of 800 million stars together with 2MASS photometry of 200 million stars (Green et al. 2015). We followed the description given in Suchomska et al. (2019). The estimated reddening from different extinction map sources shows a substantial disagreement with the result determined from Haschke et al. (2011) colour calibrations. Although there are many reasons that could be discussed, differences between the reddening values can be caused by heterogeneous distribution of the interstellar matter, particularly in the plane of the Galactic disc and towards the centre of the Milky Way. We therefore agreed to adopt the reddening values derived based on the calibration on the basis of *OGLE* data alone (Table 2).

#### 4.4.2 *Distance*

After calculating interstellar extinction parameters, it turns out that measuring the distance to the systems is an interesting problem. For this problem, we prefer two approaches for the definition of the distance to systems. One is direct measurement using the bolometric flux scaling method, and in the other the precisely calibrated relation between the surface brightness and $(V–K)$ colour of systems (Di Benedetto 2005) is used to determine their angular sizes from optical ($V$) and near-infrared ($K$) photometric calibration for cool stars.

In the first approach, a distance modulus is calculated using each system's extinction-corrected (determined in Section 4.4.1) observed magnitude and absolute $V$-band magnitude. The value of $M_V$ is calculated using the derived physical parameters of the components; a bolometric correction ($BC_V$) was computed using the observed colours and surface gravities according to several sources in the JKTABSDIM code. Following this procedure for the systems, we obtained a distance modulus for each system; these are given in Table 2.

Another approach is using the calibration of the relation between surface brightness and colour, which was recently measured with about 2 per cent accuracy (Di Benedetto 2005). Pietrzyński et al. (2019) have recently constrained the LMC distance to 1 per cent, applying surface brightness and colour to 20 eclipsing binaries. For our late-type eclipsing binary stars, we can use the very accurately calibrated relation between their surface brightness and $(V–K)$ colour to assign their angular sizes from optical ($V$) and near-infrared ($K$) photometry. Due to this surface brightness and colour relation, angular sizes of the components can be derived directly from the definition of the surface brightness. For that reason, we can measure the distance from the combination of the angular sizes of components derived in this way and the corresponding linear dimensions of the components obtained from photometric and spectroscopic analysis. The angular diameter of a star predicted by the surface brightness and colour relation is

$$\theta = 10^{0.2(S-m_0)},$$

where $S$ is the surface brightness in a given band and $m_0$ is the unreddened magnitude of a given star in this band. The distance in parsec then follows directly from angular diameter scaling and is given by a simple linear equation:

$$d[\mathrm{pc}] = 9.300\frac{R[\mathrm{R}_\odot]}{\theta[\mathrm{mas}]}.$$

In Fig. 4 we compare our late-type eclipsing binaries with the surface brightness and colour relation of Pietrzyński et al. (2019). The solid line over the black plus symbols is the fit of the relation of long-period, fully detached eclipsing binary systems in the LMC. Extinction-corrected magnitudes of the components were adjusted utilizing the light ratios from Table 2, in the manner of individual stars. We calculated the $S_V$ parameters using the same methodology for our targets. The distances $d$ (in kpc) were calculated from the equation with the values given in Table 2. The distance to the systems was presumed to be an average of the distances calculated to both components. Throughout this article, we considered a distance to the LMC of 49.6 kpc (Di Benedetto 2005) and this corresponds to a true distance modulus of $(m–M) = 18.452$. If we extend the fit of the data to the smaller $(V–K)_0$ values, the majority of our systems

[7] https://www.astro.keele.ac.uk/jkt/codes/jktabsdim.html
[8] http://dc.zah.uni-heidelberg.de/mcx

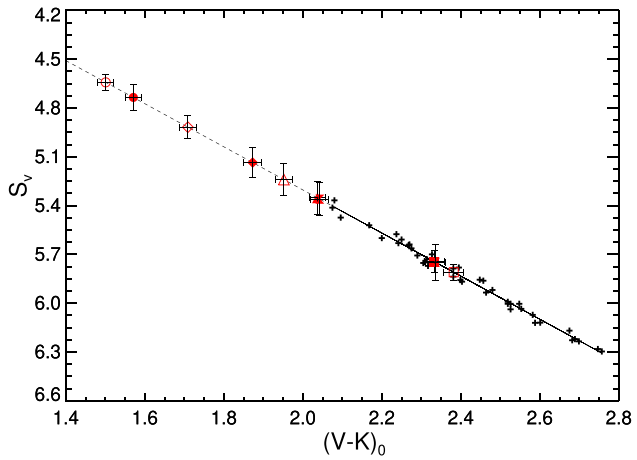


**Figure 4.** Relation between surface brightness $S_V$ and $(V-K)_0$ colour. The plot of $S_V$ versus $(V-K)_0$ (bold plus symbols) and fitted solid line come from Pietrzyński et al. (2019). Other symbols are components of systems with errors corresponding to the uncertainty of the reddening estimation.

agree within the fit. Our data also including SMC systems appear to confirm the relation. The accuracy of distance determinations based on our surface brightness and colour relation can be verified with Galactic eclipsing binaries.

## 5 EVOLUTIONARY STATUS

The evolutionary status of red giants in eclipsing binaries is not clearly understood and some discrepancies usually exist between observations and models. Over the course of a studied system's life, all components in binaries have evolved approximately in tandem to reach the configuration we observe today. In order to understand the evolutionary stage of the systems investigated, we made a comparison of the observed properties of the components with the PAdova and TRieste Stellar Evolution Code (PARSEC) stellar evolution models in Fig. 5. The PARSEC models (Bressan et al. 2012; Girardi et al. 2000; Chen et al. 2014) are available in three different versions (v1.0, v1.1, v1.2S), each of which makes substantially different predictions regarding the mass–radius diagrams, Hertzsprung–Russell (H–R) diagrams and pre-main-sequence stars. We used the latest version (v1.2S) of the models to make the comparison on the $T_{\rm eff}$ versus $L$ and $g$ planes. All models assume [Fe/H] $= -0.4$ composition for this set, followed by the relation $Y = 0.2485 + 1.78Z$ and metal content $Z = 0.006$. Where possible, we used our own estimates of [$M$/H], assuming that it is equal to [Fe/H] from the spectral analysis.

The tracks are coherent within the errors with our results for five systems, but there are a few points that have to be emphasized. Although each system consists of two almost equal-mass giants, the other physical parameters are different. We attribute this difference in physical parameters mostly to the different metallicities of spectroscopically measured values or different ages of the systems. The metallicities, especially the spectroscopic values, show a large scatter. However, it is feasible to discern some general outcomes. On average, the metallicity of the intermediate-age stars (older than about 0.6 Gyr) is significantly smaller than the metallicity of the younger population in the LMC. This inference is parallel to the results obtained from the analysis of field red giant stars in the LMC (Harris & Zaritsky 2009), where the maximum metallicity coincides with the peak of star formation in the LMC at about 0.5 Gyr, with a slow evolution of metallicity before that time.

Another quite important parameter is age. Age can be hard to limit, particularly for red giant stars in eclipsing binaries. Inferred ages can be significantly dissimilar for the different close masses of the components for a binary resulting from the analysis of photometric and spectroscopic data, as shown in Table 2. In fact, the question that we aim to answer here is: to what precision should [Fe/H] and $T_{\rm eff}$ be obtained to derive stellar ages of red giant stars? To answer this question, we should investigate the impact of eclipsing binary components more.

Alongside the picture of the stellar evolution model, it is inevitable to consider how each star has affected the other over time. When the components of the systems investigated reach the tip of the red giant branch, they have the radii given in Table 2, which are still significantly smaller than the periastron separation ($r_{\rm peri} = (1 - e)\, a$). We therefore never expect the stars to experience a common envelope phase; also, this cannot be used to constrain the present evolutionary state.

In order to estimate how tidal forces modify orbital eccentricity, we follow the theory of the equilibrium tide first proposed by Zahn (1977) to calculate a time-scale for orbit circularization ($\tau_{\rm circ}$) as a star evolves (for a review of tidal forces in stars, see Ogilvie 2014). From the equations in Zahn (1977), the time-scales $\tau_{\rm circ}$ on which orbital circularization occurs are given in Table 2 for each system.

Frankly, the high eccentricities of our current samples prove that current tidal theory cannot explain orbital evolution fully (Fig. 6). The tidal circularization time for our close red giant binaries is related to the average variation of the stellar absolute parameters, yet eccentric orbits are not uncommon. This suggests that orbital eccentricity is maintained or changed in long-orbital-period evolved binaries by some unknown mechanism. Usually, two of the strongest proposed mechanisms are mass transfer in binary systems at periastron (Soker 2000) and further interaction with the binary system (circumbinary disc or fallback material) proposed by Artymowicz et al. (1991). Both of these proposed mechanisms are tested observationally by the signatures of circumstellar matter or accretion investigated in this study. We indicated that our samples show no evidence of an emission line in their spectra that would indicate enhanced circumstellar or circumbinary dust. In this way, we prove that there is no observed evidence for mass loss or discs in these binary systems.

By modelling eccentric red giant binaries using spectroscopic and photometric data, we have figured out complete orbital solutions for these poorly understood stars. These results can be of use as input for future hydrodynamic modelling to determine how eccentricity is maintained in these stars and in other evolved eccentric binaries, possibly by mass transfer.

## 6 CONCLUSIONS

Accurate physical parameters for RG/EBs stars are still lacking and the analysis of such stars in binary systems provides a very good means of study of their properties and evolution. Except for a classification of binary type, neither of these attributes has been analysed so far and their physical properties were not known previously.

The present work is an endeavour to characterize double red giant eclipsing binary systems properly with a combination of dynamical modelling, stellar atmosphere modelling and radial velocity curves and full sets of orbital and physical parameters, and to search for the roles of tidal forces, age and stellar evolution in creating

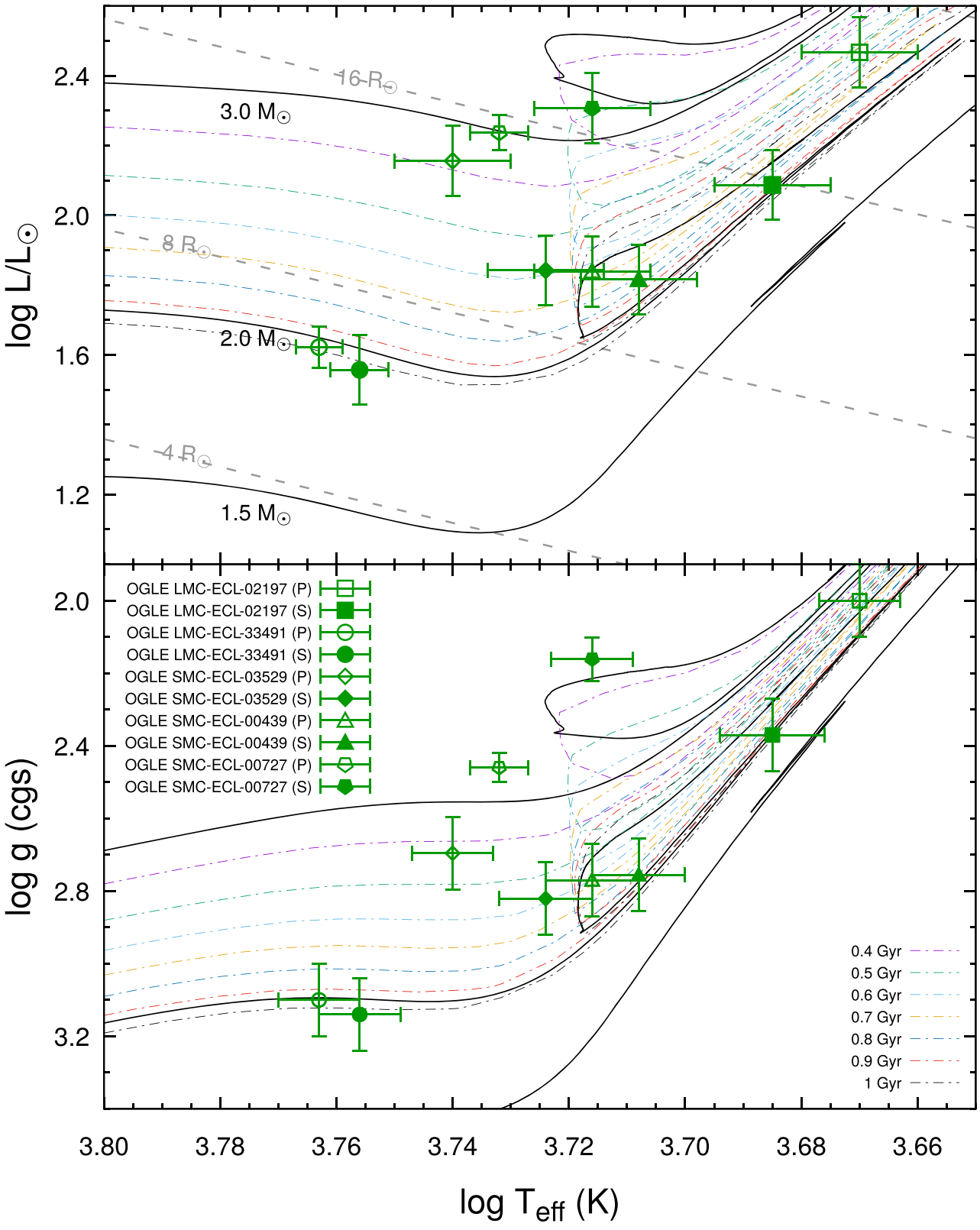


**Figure 5.** Position on the Hertzsprung–Russell diagram of the analysed RG/EBs with their components on a grid of evolutionary tracks of PARSEC models for masses 1.5–3.0 $M_{\odot}$.

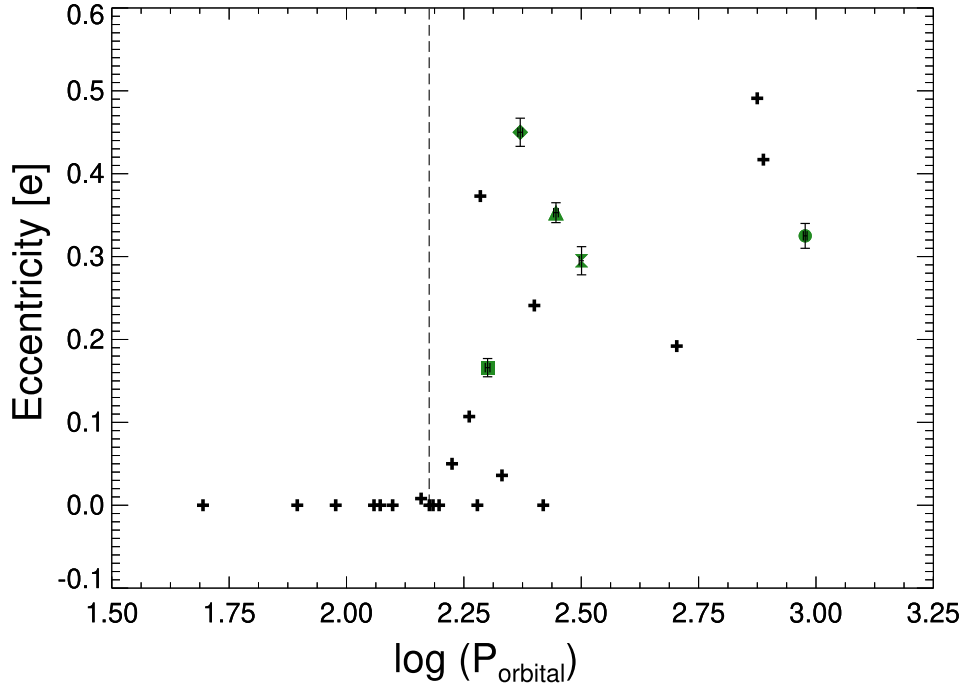


**Figure 6.** Orbital period–eccentricity diagram for known red giants in eclipsing binaries in LMC. This figure is based on fig. 8 from Graczyk et al. (2018), adding the new red giants in eclipsing binaries examined in this study (see Graczyk et al. 2018 for a table of the parameters of all published red giants). The vertical dashed line corresponds to an orbital period of 150 days.

the system we observe today. We obtained masses and radius values with uncertainties of 2–4 and 6–8 per cent, respectively, for all systems with components in slightly different phases of evolution. Such precision could make these systems useful test beds for empirical confirmation of stellar evolution models. In spite of this high precision, finding a consistent solution for more evolved systems proved non-trivial. Even though seismology allows us to constrain the properties of red giants, due to the lack of high-precision photometry we did not look for oscillations in these systems.

Average sufficient phase coverage of the radial velocities made it feasible to perform spectral disentangling and spectral analysis independently, yielding effective temperatures and metallicities of the system components. Surface gravities from the disentangled spectra and light-curve analysis nearly agree, while surface gravities from stellar evolutionary modelling are slightly different. A similar discrepancy has been found between the stellar evolutionary models and spectroscopic surface gravities of other giant stars (Graczyk et al. 2018), but the physical cause is still unknown.

The present work also makes an effort to infer properly very precise individual distance determinations for a total of five systems using the bolometric flux scaling method and surface brightness–colour relation. Distances of the systems are measured to be 40–60 kpc, with a fractional accuracy better than 4 per cent. Eclipsing binaries are located relatively far from the barycentre of the LMC and SMC. Their positions are very important. Because of this, the distance determination of our samples subserves as an excellent check of the consistency of the brightness–colour relation calibration method and the assumed spatial orientation of the LMC disc (van Marel's model: van der Marel & Cioni 2001). Such samples will allow a significant improvement in accuracy of the distance to the LMC and thus the zero-point of the cosmic distance scale. Detailed studies of the handful of known RG/EBs are crucial to ensure that we understand these extragalactic beacons.

## ACKNOWLEDGEMENTS

This research made use of data collected at ESO under programmes 094.D-0056(A), 095.D-0424(A), 097.D-0150(A), 0100.D-0273(A) (by W. Gieren), 092.D-0363(A), 096.D-0425(A), 097.D-0400(A), 098.D-0263(A), 0100.D-0339(A) and 0100.D-0339(B) (by G. Pietrzynski). This work is based on data from the *OGLE* mission. *OGLE* was competitively selected as the tenth Discovery mission. Funding for this mission is provided by NASA's Science Mission Directorate. The authors express their sincere thanks to an anonymous referee, whose valuable comments led to an improvement of the article. The following internet-based resources were used in the research for this article: the NASA Astrophysics Data System and the SIMBAD database operated at CDS, Strasbourg, France.

## REFERENCES

Artymowicz P., Clarke C. J., Lubow S. H., Pringle J. E., 1991, ApJ, 370, L35
Beck P. G. et al., 2014, A&A, 564, A36
Bessell M. S., Castelli F., Plez B., 1998, A&A, 333, 231
Blanco-Cuaresma S., Soubiran C., Heiter U., Jofré P., 2014, A&A, 569, A111
Bressan A., Marigo P., Girardi L., Salasnich B., Dal Cero C., Rubele S., Nanni A., 2012, MNRAS, 427, 127
Cayrel de Strobel G., 1969, in Gingerich O., ed., Proc.3rd Harvard-Smithsonian Conf. on Stellar Atmospheres, Massachusetts Institute of Technology Press, Cambridge, Massachusetts, p. 35
Chen Y., Girardi L., Bressan A., Marigo P., Barbieri M., Kong X., 2014, MNRAS, 444, 2525

Claret A., 2000, A&A, 363, 1081
Di Benedetto G. P., 2005, MNRAS, 357, 174
Foreman-Mackey D., 2016, JOSS, 1, 24
Fuhrmann K., Pfeiffer M., Frank C., Reetz J., Gehren T., 1997, A&A, 323, 909
Gaulme P. et al., 2016, ApJ, 832, 121
Gaulme P., McKeever J., Rawls M. L., Jackiewicz J., Mosser B., Guzik J. A., 2013, ApJ, 767, 82
Gaulme P., Jackiewicz J., Appourchaux T., Mosser B., 2014, ApJ, 785, 5
Girardi L., Bressan A., Bertelli G., Chiosi C., 2000, A&AS, 141, 371
Graczyk D. et al., 2018, ApJ, 860, 1
Gray D. F., 2005, The Observation and Analysis of Stellar Photospheres, 3rd edn. Cambridge Univ. Press, Cambridge
Gray R. O., Corbally C. J., 1994, AJ, 107, 742
Green G. M. et al., 2015, ApJ, 810, 25
Grevesse N., Asplund M., Sauval A. J., 2007, Space Sci. Rev., 130, 105
Gustafsson B., Edvardsson B., Eriksson K., Jørgensen U. G., Nordlund Å., Plez B., 2008, A&A, 486, 951
Harris J., Zaritsky D., 2009, AJ, 138, 1243
Haschke R., Grebel E. K., Duffau S., 2011, AJ, 141, 158
Hekker S. et al., 2010, ApJ, 713, L187
Hoyman B., Özdarcan O., Dervişoğlu A., Yontan T., Çakırlı Ö., 2019, New Astron., 68, 10
Ilijic S., 2004, in Hilditch R. W., Hensberge H., Pavlovski K., eds, ASP Conf. Ser. Vol. 318, Spectroscopically and Spatially Resolving the Components of the Close Binary Stars. Astron. Soc. Pac., San Francisco, p. 107
Ilijic S., Hensberge H., Pavlovski K., Freyhammer L. M., 2004, in Hilditch R. W., Hensberge H., Pavlovski K., eds, ASP Conf. Ser. Vol. 318, Spectroscopially and Spatially Resolving the Components of the Close Binary Stars. Astron. Soc. Pac., San Francisco, p. 111
Kopal Z., 1950, Harvard College Observatory Circular, 454, 1
Nelson B., Davis W. D., 1972, ApJ, 174, 617
Ogilvie G. I., 2014, ARA&A, 52, 171
Pawlak M. et al., 2016, Acta Astron., 66, 421
Pietrzyński G. et al., 2019, Nature, 567, 200
Pilecki B. et al., 2013, MNRAS, 436, 953
Pilecki B. et al., 2015, ApJ, 806, 29
Popper D. M., 1984, AJ, 89, 132
Popper D. M., Etzel P. B., 1981, AJ, 86, 102
Ruciński S. M., 1969, Acta Astron., 19, 245
Ryabchikova T., Piskunov N., Kurucz R. L., Stempels H. C., Heiter U., Pakhomov Y., Barklem P. S., 2015, Phys. Scripta, 90, 054005
Schlafly E. F., Finkbeiner D. P., 2011, ApJ, 737, 103
Sheminova V. A., 2019, Kinematics and Physics of Celestial Bodies, 35, 129
Simkin S. M., 1974, A&A, 31, 129
Soker N., 2000, A&A, 357, 557
Southworth J., Clausen J. V., 2007, A&A, 461, 1077
Southworth J., Zucker S., Maxted P. F. L., Smalley B., 2004, MNRAS, 355, 986
Southworth J., Maxted P. F. L., Smalley B., 2004, MNRAS, 351, 1277
Southworth J., Maxted P. F. L., Smalley B., 2005, A&A, 429, 645
Suchomska K. et al., 2019, A&A, 621, A93
Tonry J., Davis M., 1979, AJ, 84, 1511
Udalski A., Szymański M. K., Szymański G., 2015, Acta Astron., 65, 1
van der Marel R. P., Cioni M.-R. L., 2001, AJ, 122, 1807
Wenger M. et al., 2000, A&AS, 143, 9
Wyrzykowski Ł., Pietrukowicz P., OGLE Collaboration, 2019, in Griffin R. E., ed., IAU Symp. 339, Southern Horizons in Time-Domain Astronomy, Cambridge University Press, Cambridge, p. 226
Zahn J.-P., 1977, A&A, 500, 121
Zaritsky D., Harris J., Thompson I. B., Grebel E. K., Massey P., 2002, AJ, 123, 855

## APPENDIX A: RADIAL VELOCITY MEASUREMENTS OF TARGETS

**Table A1.** Radial velocity measurements of the targets.

| System | BJD (+240 0000) | $v_1$ (km s$^{-1}$) | $\sigma_1$ (km s$^{-1}$) | $v_2$ (km s$^{-1}$) | $\sigma_2$ (km s$^{-1}$) | S/N[a] | Instrument |
|---|---|---|---|---|---|---|---|
| OGLE LMC-ECL-02197 | 57360.29041 | 251.7 | 0.2 | 303.2 | 0.2 | 15.3 | UVES |
| | 57360.29044 | 251.0 | 0.2 | 302.0 | 0.2 | 2.6 | UVES |
| | 57658.28638 | 305.4 | 0.2 | 243.7 | 0.2 | 10.3 | UVES |
| | 57658.28643 | 304.7 | 0.2 | 242.6 | 0.2 | 1.7 | UVES |
| | 57727.29699 | 251.1 | 0.2 | 303.7 | 0.2 | 5.7 | UVES |
| | 57727.29702 | 251.0 | 0.2 | 302.4 | 0.2 | 0.7 | UVES |
| | 57728.22964 | 251.0 | 0.2 | 303.6 | 0.2 | 10.9 | UVES |
| | 57728.22969 | 250.6 | 0.2 | 303.2 | 0.2 | 1.9 | UVES |
| | 58062.22301 | 306.3 | 0.2 | 243.6 | 0.2 | 12.6 | UVES |
| | 58062.22313 | 304.6 | 0.2 | 242.7 | 0.2 | 1.8 | UVES |
| | 58083.26826 | 296.8 | 0.2 | 252.8 | 0.2 | 15.1 | UVES |
| | 58083.26837 | 296.4 | 0.2 | 252.1 | 0.2 | 3.1 | UVES |
| OGLE LMC-ECL-33491 | 57642.34461 | 289.1 | 0.2 | 248.6 | 0.1 | 13.5 | UVES |
| | 57642.34461 | 289.1 | 0.2 | 248.0 | 0.1 | 13.5 | UVES |
| | 57658.36469 | 289.2 | 0.1 | 247.4 | 0.1 | 13.1 | UVES |
| | 57658.36469 | 289.6 | 0.2 | 247.1 | 0.1 | 13.1 | UVES |
| | 58062.33471 | 258.9 | 0.1 | 276.8 | 0.1 | 11.0 | UVES |
| | 58062.33471 | 259.7 | 0.2 | 276.4 | 0.1 | 11.0 | UVES |
| | 58083.32671 | 258.7 | 0.1 | 278.5 | 0.1 | 18.2 | UVES |
| | 58083.32671 | 259.1 | 0.1 | 277.7 | 0.1 | 18.2 | UVES |
| | 58098.15199 | 256.9 | 0.4 | 277.4 | 0.1 | 2.7 | HARPS |
| | 58098.15199 | 257.8 | 0.5 | 277.2 | 0.1 | 2.7 | HARPS |
| | 58100.31538 | 258.1 | 0.1 | 279.2 | 0.1 | 14.6 | UVES |
| | 58100.31538 | 258.7 | 0.1 | 278.4 | 0.1 | 14.6 | UVES |
| | 58139.23271 | 258.0 | 0.9 | 279.2 | 0.3 | 1.4 | HARPS |
| | 58139.23271 | 258.1 | 0.8 | 279.3 | 0.2 | 1.4 | HARPS |
| | 58146.11175 | 256.6 | 1.4 | 279.3 | 0.4 | 1.7 | HARPS |
| | 58146.11175 | 257.1 | 1.6 | 280.0 | 0.3 | 1.7 | HARPS |
| OGLE SMC-ECL-03529 | 57269.74555 | 160.3 | 0.2 | 195.0 | 0.2 | 8.1 | UVES |
| | 57269.74555 | 160.4 | 0.2 | 193.7 | 0.2 | 8.1 | UVES |
| | 57270.66569 | 160.1 | 0.2 | 195.0 | 0.2 | 9.6 | UVES |
| | 57270.66569 | 159.6 | 0.2 | 193.4 | 0.2 | 9.6 | UVES |
| | 57624.63940 | 198.9 | 0.2 | 153.4 | 0.2 | 9.1 | UVES |
| | 57624.63940 | 199.1 | 0.2 | 151.8 | 0.2 | 9.1 | UVES |
| | 57642.72238 | 222.5 | 0.2 | 129.1 | 0.2 | 10.9 | UVES |
| | 57642.72238 | 222.5 | 0.2 | 128.7 | 0.2 | 10.9 | UVES |
| | 57658.58473 | 209.1 | 0.2 | 143.2 | 0.2 | 10.9 | UVES |
| | 57658.58473 | 208.8 | 0.2 | 142.9 | 0.2 | 10.9 | UVES |
| | 57658.58478 | 207.6 | 0.2 | 142.6 | 0.2 | 3.5 | UVES |
| | 58100.63122 | 209.5 | 0.2 | 142.0 | 0.2 | 10.7 | UVES |
| | 58100.63122 | 209.4 | 0.2 | 141.9 | 0.2 | 10.7 | UVES |
| OGLE SMC-ECL-00439 | 57624.16690 | 151.6 | 0.1 | 102.9 | 0.1 | 10.0 | UVES |
| | 57624.16690 | 151.3 | 0.1 | 102.3 | 0.1 | 10.0 | UVES |
| | 57642.11635 | 162.8 | 0.1 | 91.2 | 0.1 | 9.3 | UVES |
| | 57642.11635 | 162.8 | 0.1 | 90.4 | 0.1 | 9.3 | UVES |
| | 57658.10525 | 163.6 | 0.1 | 91.7 | 0.1 | 4.8 | UVES |
| | 57658.10525 | 162.9 | 0.1 | 91.0 | 0.1 | 4.8 | UVES |
| | 58062.07337 | 108.5 | 0.1 | 146.4 | 0.1 | 8.5 | UVES |
| | 58062.07337 | 108.2 | 0.1 | 145.8 | 0.1 | 8.5 | UVES |
| | 58083.13847 | 110.7 | 0.1 | 143.5 | 0.1 | 11.2 | UVES |
| | 58083.13847 | 110.8 | 0.1 | 143.1 | 0.1 | 11.2 | UVES |
| | 58100.08612 | 112.8 | 0.1 | 141.2 | 0.1 | 7.5 | UVES |
| | 58100.08612 | 114.1 | 0.1 | 139.9 | 0.1 | 7.5 | UVES |
| OGLE SMC-ECL-00727 | 57270.71756 | 133.0 | 0.2 | 177.9 | 0.2 | 5.4 | UVES |
| | 57270.71762 | 133.2 | 0.2 | 177.7 | 0.2 | 1.0 | UVES |
| | 57270.73209 | 133.1 | 0.2 | 178.2 | 0.2 | 5.8 | UVES |

**Table A1** – *continued*

| System | BJD (+240 0000) | $v_1$ (km s$^{-1}$) | $\sigma_1$ (km s$^{-1}$) | $v_2$ (km s$^{-1}$) | $\sigma_2$ (km s$^{-1}$) | S/N[a] | Instrument |
|---|---|---|---|---|---|---|---|
| | 57270.73209 | 131.9 | 0.2 | 177.9 | 0.2 | 1.1 | UVES |
| | 57642.64582 | 139.7 | 0.2 | 167.3 | 0.2 | 3.5 | UVES |
| | 58062.51678 | 170.8 | 0.2 | 125.3 | 0.2 | 8.3 | UVES |
| | 58083.66979 | 164.3 | 0.2 | 137.8 | 0.2 | 12.9 | UVES |
| | 58083.66984 | 164.1 | 0.2 | 137.0 | 0.2 | 2.9 | UVES |

[a]S/N values have been obtained from headers.

This paper has been typeset from a TEX/LATEX file prepared by the author.